Violation of centrosymmetry in time-resolved coherent x-ray diffraction from rovibrational states of diatomic molecules

Hua-Chieh Shao and Anthony F. Starace

Phys. Rev. A **99**, 033413 — Published 18 March 2019

DOI: 10.1103/PhysRevA.99.033413

Violation of centrosymmetry in time-resolved coherent x-ray diffraction from ro-vibrational states of diatomic molecules

Hua-Chieh Shao and Anthony F. Starace
Department of Physics and Astronomy, The University of Nebraska, Lincoln, Nebraska 68588-0299, USA
(Dated: February 11, 2019)

Owing to increasing applications of time-resolved coherent x-ray scattering for the investigation of molecular reaction dynamics, we develop a theoretical model for time-dependent x-ray diffraction from molecular and/or electronic motion in molecules. Our model shows that the violation of centrosymmetry (VOC) is a general phenomenon in time-resolved diffraction patterns. We employ our theoretical model to illustrate the VOC in time-resolved coherent x-ray diffraction from two oriented diatomic molecules undergoing ro-vibrational motion: lithium hydride (LiD) and hydrogen (HD). Our simulations show asymmetric x-ray diffraction images that reflect the directions of the molecular motions.

I. INTRODUCTION

Recent technological advances have enabled the generation of intense, short, coherent x-ray radiation using synchrotrons [1–3], laser-driven plasmas [4–6], and free-electron lasers [7–9]. Consequently, various aspects of x-ray physics and chemistry have been explored with these new x-ray sources [10, 11]. For example, following ionization by intense x-rays, the ensuing dynamics in atoms [12–14], molecules [15–17], and clusters [18, 19] have been studied. In this regard, absorption [20, 21], stimulated emission [22–24], and photoelectron [25–27] spectroscopies have been shown to provide element-specific probes for studying these electronic and structural dynamics. Coherent x-ray diffraction [28–31], in particular, has long been used to determine the microscopic structures of molecules, solids, and proteins because of its ångström resolution and deep penetration depth [32]. With the recent development of femtosecond (fs) x-ray sources, time-resolved coherent x-ray diffraction (using a pump-probe scheme) has been shown capable of directly imaging the transient structures along a reaction path [33–42], thereby providing deeper insight into the underlying reaction mechanisms. Theories have also been developed to simulate and interpret the time-resolved diffraction images in terms of target electronic or molecular motions [43–49].

Regarding the theoretical treatment of non-resonant coherent x-ray diffraction, we emphasize that there is a nontrivial distinction between the time-independent and the time-dependent descriptions. Namely, while the diffraction images in a time-independent treatment are centrosymmetric, as prescribed by Friedel's law [50], this is not necessarily the case in a time-dependent treatment. Specifically, in the theory of time-independent high-energy scattering, the elastic x-ray scattering amplitude $F(\boldsymbol{q})$ to first-order in the interaction (*i.e.*, in the kinematical approximation) is proportional to the Fourier transform of the electron density $\rho_e(\boldsymbol{x})$ (*i.e.*, the molecular form factor):

$$F(\boldsymbol{q}) \propto \int d\boldsymbol{x}\, e^{i\boldsymbol{q}\cdot\boldsymbol{x}}\, \rho_e(\boldsymbol{x})\,, \tag{1}$$

where $\boldsymbol{q}$ is the momentum transfer. Consequently, $F(-\boldsymbol{q}) = F^*(\boldsymbol{q})$ and the differential cross section, which is the absolute square of the scattering amplitude, is always centrosymmetric, even if $\rho_e(\boldsymbol{x})$ lacks any symmetry. The violation of centrosymmetry (VOC) in non-resonant diffraction images has been found in simulations focused on the detection of electron motion in the hydrogen atom [47, 51, 52]. In this paper we show, using the same level of approximation as in time-independent theories, that VOC is a general phenomenon in time-resolved coherent x-ray diffraction. In particular, we show that evidence of VOC in time-resolved coherent x-ray diffraction images does not originate only from electron motion, but stems also from molecular vibrational motion.

In order to illustrate VOC features in diffraction images, we have developed a model for time-resolved coherent x-ray diffraction from nuclear and/or electronic motion in a molecule. This model is adapted from the time-dependent theory of ultrafast electron diffraction [51, 53]. However, for the sake of completeness, the full details of the model as applied to the case of a molecule are presented in Sec. II. The details of applying this model to the case of oriented ro-vibrational motion of a diatomic molecule are given in Sec. III. In particular, we assume the molecular motion is initiated by some pump procedure that impulsively excites an electron from the ground state to some excited state, so that the internuclear distances in the molecule remain unchanged during the pump process (*i.e.*, we use the Franck-Condon principle [54]). After the excitation, the molecule begins its ro-vibrational motion, and this motion is then imaged using time-delayed, coherent fs x-ray pulses. Our results for the LiD and HD diatomic molecules are given in Sec. IV. In both cases, the x-ray diffraction images show the VOC resulting from the molecular motion. We conclude with a summary and discussion of our results in Sec. V.

Before presenting our model for time-resolved coherent x-ray diffraction, some brief remarks on our terminology are necessary. We use the term "coherent x-ray diffraction" to refer to the coherence properties of the x-ray pulses themselves. Specifically, the term means that the off-diagonal elements of the density matrix describing the x-ray pulses in reciprocal space are nonzero, denot-

ing either full or partial coherence, so that the frequency components of the pulses maintain their mutual phase relations to some degree. This usage differs from that in some of the older literature concerning time-independent x-ray diffraction or crystallography, in which coherence may refer to the scattering mechanism. Namely, coherent and incoherent x-ray scattering are often used to stand for Rayleigh (elastic) and Compton (inelastic) scattering, respectively (see, *e.g.*, [55, 56]). In our model, both types of scattering are included and both contribute to the time-resolved diffractive interference patterns we calculate owing to the bandwidth of short x-ray pulses, which allows both elastic and inelastic processes differing in energy to interfere.

II. THEORETICAL FORMULATION

The essential ideas for modeling time-dependent x-ray scattering are summarized here, and details regarding the implementation of these ideas in our theoretical formulation are presented in the following subsections. In order to properly describe time-dependent coherent x-ray scattering, the x-ray radiation and the molecular target must be localized in both space and time in order that the centroid of motion of the x-ray pulse, the center of mass of the target, and the collision time can all be well-defined. The x-ray pulse and the molecule are localized using *wave-packet integrals* that coherently superpose their momentum components to form wave packets [57]. In order to properly account for the recoil of the x-ray photon (*i.e.*, for Compton scattering) and the exchange of energy between the photon and the molecule (which has been shown to be important for describing time-dependent scattering from targets in which electrons are moving [47, 51]), we employ a field quantization description of the x-ray radiation [58]. After formulating the localized wave packets for the initial states of the x-ray pulse and the molecule, these wave packets are propagated in time and the x-ray diffraction patterns resulting from the internal molecular motions are calculated.

Finally, our formulation is given in the interaction picture, and atomic units (a.u.), $\hbar = e = m_e = 1$, are used throughout this paper unless specified otherwise.

A. Time-dependent x-ray scattering

Consider an x-ray photon γ with momentum $\boldsymbol{k}_0$ that scatters from a molecule M having momentum $\boldsymbol{k}_a$,

$$\gamma(\boldsymbol{k}_0, \lambda_0) + M^*(\boldsymbol{k}_a, a) \to \gamma(\boldsymbol{k}_1, \lambda_1) + M^*(\boldsymbol{k}_b, b)\,, \quad (2)$$

where $\boldsymbol{k}_1$ and $\boldsymbol{k}_b$ are the respective momenta of the photon and the molecule after the collision, λ_0 and λ_1 label the respective polarizations of the incident and scattered photons, and the quantum numbers characterizing the molecular states before and after the scattering are collectively symbolized by a and b, respectively. The molecule involves some internal nuclear (and/or electronic) motion that is imaged by the x-ray pulse (whose pulse length is short compared to the period of the internal motion).

Let Hamiltonian of the scattering system be

$$H = H_M + H_\gamma + V\,, \quad (3)$$

where H_M and H_γ are the respective Hamiltonians of the molecule and the electromagnetic radiation, and V is the interaction between the x-ray photons and the charged particles in the molecule. For the case of non-relativistic electron dynamics, the interaction V in the Coulomb gauge comprises two terms that are proportional to $\boldsymbol{A}\cdot\boldsymbol{p}$ and $\boldsymbol{A}^2$, respectively. Here, $\boldsymbol{A}$ is the vector potential of the x-ray radiation, and $\boldsymbol{p}$ is the canonical momentum of a charged particle in the molecule. However, for x-ray scattering in which the radiation frequency is much higher than the binding energies of the charged particles (*i.e.*, non-resonant scattering), the $\boldsymbol{A}^2$ term dominates the interaction. Thus, we retain only this term in V:

$$V(t) \simeq \frac{1}{2m_e c^2} \int d\boldsymbol{x}\, \boldsymbol{\psi}^\dagger(\boldsymbol{x}, t)\, \boldsymbol{A}^2(\boldsymbol{x}, t)\, \boldsymbol{\psi}(\boldsymbol{x}, t)\,, \quad (4)$$

where m_e is the mass of electron, c is the speed of light, and $\boldsymbol{\psi}(\boldsymbol{x}, t)$ is the (annihilation) field operator for the electrons in the molecule satisfying the equal-time anti-commutation rule, $\{\boldsymbol{\psi}(\boldsymbol{x}', t),\, \boldsymbol{\psi}^\dagger(\boldsymbol{x}, t)\} = \delta(\boldsymbol{x}' - \boldsymbol{x})$. For the sake of clarity, the spin index of $\boldsymbol{\psi}(\boldsymbol{x}, t)$ is suppressed because photons do not directly couple to the electrons' spin degrees of freedom, though the spin statistics is still implied implicitly in our formulations. The scattering of the photon from the nuclei in the molecule is also neglected in Eq. (4) owing to the much greater masses of the nuclei as compared to the electron mass.

For x-ray photon frequencies much above the K ionization edges of the constituent atoms in the molecule, first-order time-dependent perturbation theory can be used to evaluate the x-ray scattering transition amplitude from an initial state i to a final state f:

$$\mathscr{T}_{fi} \simeq \int dt\, \langle \psi_f |\, V(t)\, | \psi_i \rangle\,, \quad (5)$$

where $|\psi_i\rangle$ is the entrance state of the reaction (2), and $|\psi_f\rangle$ is the final state of an exit channel detected in a measurement.

Having thus formulated an expression for the transition amplitude $\mathscr{T}_{fi}$, we turn now to describing the entrance and exit states, $|\psi_i\rangle$ and $|\psi_f\rangle$, in Secs. II B and II C respectively below.

B. Entrance states

The entrance state of the scattering system is written as a direct product of the x-ray and molecular states:

$$|\psi_i\rangle = |\alpha_0\rangle \otimes |\psi_a\rangle\,. \quad (6)$$

A coherent state basis is employed to describe the entrance state $|\alpha_0\rangle$ of the x-ray pulse for the following reasons. First, a coherent state is a quantized radiation state (*i.e.*, a photon field state) produced by a classical current distribution [59], and many x-ray radiation processes can be modeled using classical electrodynamics [5, 9, 60]. Second, diffraction experiments involve a large and indefinite number of photons, which cannot be described by a single configuration of photon occupation numbers. Third, a coherent-state representation renders a momentum interpretation of the x-ray scattering that aids interpretation of the time-resolved diffraction images (see Sec. II F). Since the incident x-ray pulses have finite duration, thus comprising a distribution of frequencies, they cannot be described by a single-mode coherent state. Accordingly, $|\alpha_0\rangle$ is modeled as a product of coherent states with different momenta and polarizations [61]:

$$|\alpha_0\rangle = \prod_{\lambda_0,\,\boldsymbol{k}_0} \big|\alpha_{\lambda_0}(\boldsymbol{k}_0)\big\rangle\,, \tag{7}$$

where $\alpha_{\lambda_0}(\boldsymbol{k}_0)$ labels the coherent state with polarization λ_0 and momentum $\boldsymbol{k}_0$. The spectrum $\alpha_{\lambda_0}(\boldsymbol{k}_0)$ of $|\alpha_0\rangle$ depends on the character of the x-ray pulse, which will be specified later (in Sec. II F). Each coherent state $|\alpha_\lambda(\boldsymbol{k})\rangle$ can be further expanded in terms of the photon number states $|n\rangle$:

$$|\alpha_\lambda(\boldsymbol{k})\rangle = \sum_{n=0}^{\infty} |n\rangle\, e^{-\frac{1}{2}|\alpha_\lambda(\boldsymbol{k})|^2}\, \frac{\alpha_\lambda^n(\boldsymbol{k})}{\sqrt{n!}}\,, \tag{8}$$

where $n \equiv n_\lambda(\boldsymbol{k})$ is the occupation number for the λ, $\boldsymbol{k}$ mode; for simplicity of notation, the mode indexes of n are suppressed here. If the x-ray pulses are mixed states, the above description can be generalized using a density-matrix formulation (see, e.g., the Supporting Information accompanying Ref. [47]).

For the entrance state $|\psi_a\rangle$ of the molecule, we assume the molecular and/or electronic motion is initiated by some pump procedure such that (i) the time zero of the motion can be defined and (ii) the ensuing evolution of the molecule can be approximately modeled as a coherent superposition state with wave function $\psi_{\rm coh}$. Assuming there are N_j particles of type j in the molecule (*e.g.*, N_e electrons, N_1 nuclei of one kind, and N_2 nuclei of another kind, *etc.*), the molecular state can be written as

$$|\psi_a\rangle = \int d\mu \prod_j \frac{1}{\sqrt{N_j!}}\, \boldsymbol{\psi}_j^\dagger(\boldsymbol{x}_1)\cdots\boldsymbol{\psi}_j^\dagger(\boldsymbol{x}_{N_j})\,|0\rangle\,\psi_{\rm coh}\,, \tag{9}$$

where $\boldsymbol{\psi}_j$ is the field operator for the jth type of particle, $|0\rangle$ is the vacuum state for all types of particle, and the integration, denoted by $d\mu$, is over the configuration space of all the particles in the molecule. The commutation rules for $\boldsymbol{\psi}_j$ depend on the spin statistics of the jth type of the particles (*i.e.*, boson or fermion).

The expression of $\psi_{\rm coh}$ is assumed to be factorized into an external part, which describes the molecule's center-of-mass motion, and an internal part, which describes the molecular steric and/or electronic motions. For the external part, we use a basis set of plane waves, χ_a, in the wave-packet integral for the center-of-mass motion:

$$\chi_a = (2\pi)^{-3/2}\, e^{i\boldsymbol{k}_a\cdot\boldsymbol{x}_a}\,, \tag{10}$$

where $\boldsymbol{k}_a$ and $\boldsymbol{x}_a$ are the momentum and center-of-mass coordinates of the molecule, respectively. For the internal part, the coherent superposition state, $\psi_{\rm coh}$, is expanded in the eigenstates of the molecular Hamiltonian. In pump-probe experiments, the time evolution of the target states is tracked by varying the delay between the pump and probe pulses, so the entrance state $|\psi_i\rangle$ is a function of the pump-probe delay. Furthermore, for gas-phase x-ray diffraction, the pump and probe times of a molecule depend on its position in the gas ensemble. In order to incorporate this delay and position dependence into the initial conditions of $|\psi_i\rangle$, we assume that the pump procedure precedes the x-ray probe pulse by a time t_d for a molecule located at the origin. Then the relative delay between the pump and probe pulses for a molecule at an arbitrary position $\boldsymbol{b}$ is accounted for by displacing the molecular wave function $\psi_{\rm coh}$ in time. In other words, the state of the x-ray pulses $|\alpha_0\rangle$ are identical for all delays, while the molecular state for the molecule at the position $\boldsymbol{b}$ is displaced in time by $t_a(\boldsymbol{b})$.

With the above considerations, the wave function for the molecule at the position $\boldsymbol{b}$ is written as

$$\psi_{\rm coh} = \int d\boldsymbol{k}_a\, a(\boldsymbol{k}_a)\, e^{-i\boldsymbol{k}_a\cdot\boldsymbol{b}}\,\chi_a \sum_n c_n\,\phi_n\, e^{-i\varepsilon_n t_a}\,, \tag{11}$$

where $a(\boldsymbol{k}_a)$ is the momentum amplitude of the wave packet, ϕ_n is an eigenstate of the molecule with energy ε_n, n [not to be confused with the photon occupation number $n_\lambda(\boldsymbol{k})$] denotes the set of quantum numbers specifying the internal molecular state (*e.g.*, rotational, vibrational, and electronic states), and c_n is the amplitude of ϕ_n for a molecule at the origin ($\boldsymbol{b} = 0$) for a zero pump-probe delay. The first part of Eq. (11) (before the summation) describes the external motion of the molecular wave packet, and the second part represents the internal molecular motion. The perpendicular component $\boldsymbol{b}_\perp$ is the impact parameter of the scattering. If one further assumes that the group velocity of the pump pulse is the speed of light and that the pump and probe pulses are co-propagating, then

$$t_a \simeq t_d - \frac{b_\parallel}{c}\,, \tag{12}$$

where $b_\parallel$ is the longitudinal component of $\boldsymbol{b}$ along the propagation direction. An average of the transition probability over the positions of molecules in the gas ensemble will be implemented later (in Sec. II E).

C. Exit states

As for the entrance state, the exit state $|\psi_f\rangle$ is written as a direct product of the photon and molecular states:

$$|\psi_f\rangle = |n_1\rangle \otimes |\psi_b\rangle\,. \tag{13}$$

However, in contrast to the entrance state, the photon state $|n_1\rangle$ of the exit channel is described using the occupation-number representation because, in typical experiments for x-ray diffraction, the measurement of diffraction patterns involves photon-counting detection. Specifically, we consider that one photon is scattered from the molecule with momentum $\boldsymbol{k}_1$ and polarization λ_1, so that

$$|n_1\rangle = \big|\{n_\lambda(\boldsymbol{k}) : \lambda, \boldsymbol{k} \in \alpha_0\}\big\rangle \otimes \big|\mathbf{1}_{\lambda_1}(\boldsymbol{k}_1)\big\rangle\,, \tag{14}$$

where the first factor, $|\{n_\lambda(\boldsymbol{k})\}\rangle$, stands for the unscattered photons in which λ and $\boldsymbol{k}$ belong to the occupied modes in the entrance state $|\alpha_0\rangle$, and the second factor, $|\mathbf{1}_{\lambda_1}(\boldsymbol{k}_1)\rangle$, indicates that only one photon is in the scattered state.

The exit state for the molecule is simply chosen as an eigenstate of the molecular Hamiltonian H_M:

$$|\psi_b\rangle = \int d\mu \prod_j \frac{1}{\sqrt{N_j!}}\, \boldsymbol{\psi}_j^\dagger(\boldsymbol{x}_1)\cdots\boldsymbol{\psi}_j^\dagger(\boldsymbol{x}_{N_j})\,|0\rangle\,\chi_b\,\phi_m\,. \tag{15}$$

where χ_b, which describes the center-of-mass motion of the molecule after the collision, is a plane-wave state with momentum $\boldsymbol{k}_b$ [similar to Eq. (10)], and ϕ_m is an internal molecular eigenstate.

D. The transition amplitude

Using the above descriptions for the entrance and exit states, the transition amplitude can be calculated. Thus, applying Eqs. (6) and (13) to the integrand of Eq. (5), one obtains the matrix element

$$\begin{aligned}\langle\psi_f|V(t)|\psi_i\rangle &\simeq \frac{1}{2m_e c^2} \\ &\times \int d\boldsymbol{x}\,\langle n_1|\boldsymbol{A}^2(\boldsymbol{x},t)|\alpha_0\rangle\,\langle\psi_b|\boldsymbol{\psi}^\dagger(\boldsymbol{x},t)\,\boldsymbol{\psi}(\boldsymbol{x},t)|\psi_a\rangle\,.\end{aligned} \tag{16}$$

To evaluate the first factor of the integrand, we first expand the vector potential $\boldsymbol{A}(\boldsymbol{x},t)$ in terms of plane-wave modes of λ and $\boldsymbol{k}$:

$$\begin{aligned}\boldsymbol{A}(\boldsymbol{x},t) = \frac{c}{2\pi}\int d\boldsymbol{k}\,\frac{1}{\sqrt{\omega}}\sum_\lambda \Big(&\boldsymbol{\epsilon}_\lambda(\boldsymbol{k})\,a_\lambda(\boldsymbol{k})\,e^{i(\boldsymbol{k}\cdot\boldsymbol{x}-\omega t)} \\ &+ \boldsymbol{\epsilon}_\lambda^*(\boldsymbol{k})\,a_\lambda^\dagger(\boldsymbol{k})\,e^{-i(\boldsymbol{k}\cdot\boldsymbol{x}-\omega t)}\Big)\,,\end{aligned} \tag{17}$$

where $\boldsymbol{\epsilon}_\lambda(\boldsymbol{k})$ is the polarization vector, $a_\lambda(\boldsymbol{k})$ is the annihilation operator for the λ, $\boldsymbol{k}$ mode, and $\omega = c\,|\boldsymbol{k}|$. The annihilation, $a_\lambda(\boldsymbol{k})$, and creation, $a_\lambda^\dagger(\boldsymbol{k})$, operators satisfy the commutation rule: $[a_{\lambda'}(\boldsymbol{k}'),\, a_\lambda^\dagger(\boldsymbol{k})] = \delta_{\lambda'\lambda}\,\delta(\boldsymbol{k}'-\boldsymbol{k})$. Then, utilizing Eqs. (7) and (14), the commutation rules for a and $a^\dagger$, and using the fact that the coherent state $|\alpha_\lambda(\boldsymbol{k})\rangle$ is an eigenstate of the annihilation operator with eigenvalue $\alpha_\lambda(\boldsymbol{k})$, *i.e.*,

$$a_\lambda(\boldsymbol{k})\,|\alpha_\lambda(\boldsymbol{k})\rangle = |\alpha_\lambda(\boldsymbol{k})\rangle\,\alpha_\lambda(\boldsymbol{k})\,, \tag{18}$$

one may show that

$$\begin{aligned}\langle n_1|\boldsymbol{A}^2(\boldsymbol{x},t)|\alpha_0\rangle = \frac{c^2}{2\pi^2}\int d\boldsymbol{k}_0\,\frac{1}{\sqrt{\omega_1\,\omega_0}} \\ \times \sum_{\lambda_0}\epsilon_{\lambda_1}^*(\boldsymbol{k}_1)\cdot\epsilon_{\lambda_0}(\boldsymbol{k}_0)\,\alpha_{\lambda_0}(\boldsymbol{k}_0)\,\langle\{n_\lambda(\boldsymbol{k})\}|\,\alpha_0\rangle \\ \times e^{i[(\boldsymbol{k}_0-\boldsymbol{k}_1)\cdot\boldsymbol{x}-(\omega_0-\omega_1)t]}\,,\end{aligned} \tag{19}$$

where $\omega_j \equiv c\,|\boldsymbol{k}_j|$ $(j=0,1)$. Note that the final state of the inner product in the integrand includes only the unscattered photons. Physically, the matrix element (19) depicts a scattering process in which, at the spacetime $\boldsymbol{x}$,t, a photon is annihilated from the coherent state $|\alpha_{\lambda_0}(\boldsymbol{k}_0)\rangle$ with amplitude $\alpha_{\lambda_0}(\boldsymbol{k}_0)$ and a photon of mode λ_1, $\boldsymbol{k}_1$ is created. The integration over $\boldsymbol{k}_0$ and the summation over λ_0 coherently superpose the transition amplitudes from all the occupied modes in $|\alpha_0\rangle$ to $|\mathbf{1}_{\lambda_1}(\boldsymbol{k}_1)\rangle$. The inner product $\langle\{n_\lambda(\boldsymbol{k})\}|\alpha_0\rangle$ takes account of the portion of the transition matrix contributed by the unscattered photons in this process.

As for the second factor in the integrand of Eq. (16), since the number of electrons in the molecule is well-defined and conserved in non-relativistic quantum electrodynamics, it is convenient to use the identity

$$\boldsymbol{\psi}(\boldsymbol{x},t) = e^{iH_M t}\,\boldsymbol{\psi}(\boldsymbol{x})\,e^{-iH_M t} \tag{20}$$

to calculate the matrix element so that the time dependence is carried by the states:

$$\langle\psi_b|\boldsymbol{\psi}^\dagger(\boldsymbol{x},t)\,\boldsymbol{\psi}(\boldsymbol{x},t)|\psi_a\rangle = \langle\psi_b(t)|\boldsymbol{\psi}^\dagger(\boldsymbol{x})\,\boldsymbol{\psi}(\boldsymbol{x})|\psi_a(t)\rangle\,. \tag{21}$$

Since the states $|\psi_a\rangle$ and $|\psi_b\rangle$ are expanded in terms of the eigenstates of the molecular Hamiltonian, their time evolution is obtained by multiplying the components of the wave functions by the time-dependent phase associated with each of the eigenstates. Substituting Eqs. (9) and (15) with the time-dependent phases into the right-hand side of Eq. (21), the matrix element (21) can be calculated as follows: First, since the interaction $V(t)$ involves only the field operators of the electrons, for the nuclei this matrix element is simply the inner product of the nuclear parts of the wave functions. Second, the electronic part can be calculated using the anti-commutation rules for $\boldsymbol{\psi}(\boldsymbol{x})$, $\boldsymbol{\psi}^\dagger(\boldsymbol{x})$ repeatedly such that all the field operators are in normal order (or, alternatively, one could apply Wick's theorem, according to which the contraction of the field operators yields δ-functions). The result

is the following identity [see also Eq. (21.59) of Ref. [62]]:

$$\begin{aligned}&\langle 0|\boldsymbol{\psi}(\boldsymbol{x}'_{N_e})\cdots\boldsymbol{\psi}(\boldsymbol{x}'_1)\,\boldsymbol{\psi}^\dagger(\boldsymbol{x}')\,\boldsymbol{\psi}(\boldsymbol{x})\,\boldsymbol{\psi}^\dagger(\boldsymbol{x}_1)\cdots\boldsymbol{\psi}^\dagger(\boldsymbol{x}_{N_e})|0\rangle\\&=\sum_{i=1}^{N_e}\sum_P \mathrm{sgn}(P)\,\delta(\boldsymbol{x}'_{N_e}-\boldsymbol{x}_{N_e})\cdots\delta(\boldsymbol{x}'-\boldsymbol{x}_i)\cdots\\&\times\cdots\delta(\boldsymbol{x}'_1-\boldsymbol{x}_1)\,\delta(\boldsymbol{x}'_i-\boldsymbol{x})\,,\end{aligned}\tag{22}$$

where P denotes a permutation of all primed coordinates except $\boldsymbol{x}'_i$, the P summation stands for summation over all permutations P, and $\mathrm{sgn}(P)=\pm1$ is positive (negative) for an even (odd) permutation P. Note that in Eq. (22) we have temporarily distinguished the coordinates $\boldsymbol{x}$ and $\boldsymbol{x}'$ of the field operators in Eq. (21); we shall set $\boldsymbol{x}=\boldsymbol{x}'$ after evaluating the matrix element (21). Applying the identity in Eq. (22) to Eq. (21), together with Eqs. (9) and (15), one obtains

$$\begin{aligned}&\langle\psi_b|\,\boldsymbol{\psi}^\dagger(\boldsymbol{x},t)\,\boldsymbol{\psi}(\boldsymbol{x},t)\,|\psi_a\rangle\\&=\int d\boldsymbol{k}_a\,a(\boldsymbol{k}_a)\,e^{-i\boldsymbol{k}_a\cdot\boldsymbol{b}}\sum_{i=1}^{N_e}\int d\mu\,\delta(\boldsymbol{x}-\boldsymbol{x}_i)\,\chi_b^*\,\chi_a\\&\times\sum_n c_n\,\phi_m^*\,\phi_n\,e^{-i\varepsilon_n t_a}\,e^{i(E_b+\varepsilon_m-E_a-\varepsilon_n)t}\,,\end{aligned}\tag{23}$$

where $\boldsymbol{x}_i$ is the coordinate of the ith electron, and E_a and E_b are the kinetic energies of the molecule in the entrance and exit channels, respectively. Note that any permutation P of electron coordinates renders identical amplitudes because the wave functions have been antisymmetrized.

Physically, the matrix element (23), without the $\boldsymbol{k}_a$ integral and the i and n summations, is the scattering amplitude for the ith electron from the state $\chi_a\,\phi_n$ to the state $\chi_b\,\phi_m$ at position $\boldsymbol{x}$ and time t. Because of the indistinguishability of electrons, the contribution to the scattering amplitude from each individual electron is superposed coherently by the i summation. In addition, as the entrance state $|\psi_a\rangle$ is a coherent superposition state, the scattering amplitude is further averaged over the contributions from the components in the wave packet, weighted by their corresponding amplitudes c_n and $a(\boldsymbol{k}_a)$, by means respectively of the sum over n and the integration over $\boldsymbol{k}_a$.

Finally, the time-resolved transition amplitude $\mathscr{T}_{fi}$ can be calculated by substituting Eqs. (16), (19) and (23) into Eq. (5). Since spacetime is homogeneous, the temporal integration yields a δ function representing the conservation of energy as well as a δ function for the conservation of total linear momentum, both of which can be factored from $\mathscr{T}_{fi}$. One obtains then

$$\begin{aligned}\mathscr{T}_{fi}\simeq\frac{1}{2\pi m_e}\int d\boldsymbol{k}_0\,\frac{1}{\sqrt{\omega_1\,\omega_0}}\sum_{\lambda_0}\epsilon^*_{\lambda_1}(\boldsymbol{k}_1)\cdot\epsilon_{\lambda_0}(\boldsymbol{k}_0)\\\times\alpha_{\lambda_0}(\boldsymbol{k}_0)\,\langle\{n_\lambda(\boldsymbol{k})\}|\,\alpha_0\rangle\int d\boldsymbol{k}_a\,a(\boldsymbol{k}_a)\,e^{-i\boldsymbol{k}_a\cdot\boldsymbol{b}}\\\times\sum_n c_n\,T_{mn}\,e^{-i\varepsilon_n t_a}\,\delta(E_f-E_i)\,\delta(\mathcal{P}_f-\mathcal{P}_i)\,,\end{aligned}\tag{24}$$

where $E_i\equiv\omega_0+\varepsilon_n+E_a$ and $E_f\equiv\omega_1+\varepsilon_m+E_b$, respectively, are the initial and final total energies, $\mathcal{P}_i\equiv\boldsymbol{k}_0+\boldsymbol{k}_a$ and $\mathcal{P}_f\equiv\boldsymbol{k}_1+\boldsymbol{k}_b$, respectively, are the initial and final total linear momenta of the scattering system, and

$$T_{mn}\simeq\sum_{i=1}^{N_e}\int d\boldsymbol{y}_i\,e^{i\boldsymbol{q}\cdot\boldsymbol{y}_i}\,(\phi_m,\phi_n)\tag{25}$$

is the usual transition matrix (or the scattering amplitude) for x-ray diffraction in the center-of-mass frame. [Note that Eq. (25) reduces to the familiar molecular form factor in the case of elastic scattering, $m=n$.] Here, $\boldsymbol{q}\equiv\boldsymbol{k}_0-\boldsymbol{k}_1$ is the momentum transfer, and the inner product in the integrand involves an integration over the internal coordinates of all particles in the molecule except for the coordinate $\boldsymbol{y}_i$ of the electron that collides with the x-ray photon. We also make use of the fact that the electron mass is much less than the nuclear masses in the molecule.

One sees that the transition amplitude, $\mathscr{T}_{fi}$, for short x-ray pulses scattered from the coherent superposition state $|\psi_a\rangle$ is a coherent superposition of the scattering amplitudes T_{mn} from each component of the wave packet weighted by the corresponding amplitudes c_n, $a(\boldsymbol{k}_a)$, and $\alpha_\lambda(\boldsymbol{k})$ satisfying the conservation of energy and momentum. It is the interference of these components that renders a delay dependence in the time-resolved scattering probability.

E. Scattering probability and ensemble average

The scattering probability involves various final-state summations and integrations over the absolute square of the time-resolved transition amplitude, $|\mathscr{T}_{fi}|^2$,

$$\mathscr{P}=\frac{1}{\langle N_\gamma\rangle}\sum_m\sum_{\{n_\lambda(\boldsymbol{k})\}}\sum_{\lambda_1}\int d\boldsymbol{k}_b\int d\boldsymbol{k}_1\,|\mathscr{T}_{fi}|^2\,,\tag{26}$$

where $\langle N_\gamma\rangle$ is the expectation value of the number of photons in the entrance state $|\alpha_0\rangle$. The first summation sums over the molecular final states; the second summation represents the final-state sum for the unscattered photons; and the last summation sums over the polarizations of the scattered photon. The first and second integrals integrate over the final momenta of the molecule and scattered photon, respectively. The ranges of these summations and integrations depend on the detection scheme of the experimental setup, which determines which subsets of these exit channels are measured. In typical x-ray diffraction experiments, the frequencies and polarizations of the scattered photons are not resolved and only the diffraction patterns are recorded as a function of pump-probe delay. In other words, the scattering intensities of the x rays are measured as functions of the scattering angles $\hat{\boldsymbol{k}}_1$ at each pump-probe delay, and these unresolved channels are summed accordingly. Therefore, we define

the differential scattering probability as:

$$\frac{d\mathscr{P}}{d\hat{\boldsymbol{k}}_1} \equiv \frac{1}{\langle N_\gamma \rangle} \sum_m \sum_{\{n_\lambda(\boldsymbol{k})\}} \sum_{\lambda_1} \int d\boldsymbol{k}_b \int d\omega_1 \, \frac{\omega_1^2}{c^3} \left| \mathscr{T}_{fi} \right|^2 , \tag{27}$$

which represents the diffraction patterns measured in time-resolved x-ray scattering.

Moreover, in gas-phase scattering the positions of the molecular targets cannot be controlled with atomic precision, so an average of $d\mathscr{P}/d\hat{\boldsymbol{k}}_1$ over the distribution of the molecular positions in an ensemble is necessary. For an ensemble having a position distribution $\rho(\boldsymbol{b})$, the ensemble-averaged differential probability (EADP) is

$$\left\langle \frac{d\mathscr{P}}{d\hat{\boldsymbol{k}}_1} \right\rangle = \int d\boldsymbol{b} \, \rho(\boldsymbol{b}) \, \frac{d\mathscr{P}}{d\hat{\boldsymbol{k}}_1} . \tag{28}$$

In the following, we present the procedures needed to calculate the EADP from the definition of the differential probability (27) and the transition amplitude (24). Moreover, to simplify the expression, assumptions and approximations frequently fulfilled in experiments are made.

For the x rays, we assume the incident pulses are linearly polarized and well-collimated, so that the paraxial approximation can be used. Thus, the polarization vector $\epsilon_{\lambda_0}(\boldsymbol{k}_0)$ is insensitive to the angular spread $\hat{\boldsymbol{k}}_0$ of the incident radiation, and hence the polarization factor can be pulled out of the $\boldsymbol{k}_0$ integral in Eq. (24).

Since no measurement is performed to discriminate the unscattered photons, the $\{n_\lambda(\boldsymbol{k})\}$-summation exhausts all possible numbers of photons $n_\lambda(\boldsymbol{k})$ in every occupied mode λ, $\boldsymbol{k}$ in $|\alpha_0\rangle$ (*i.e.*, all configurations for the occupation numbers of the exit state $\big|\{n_\lambda(\boldsymbol{k}) : \lambda, \boldsymbol{k} \in \alpha_0\}\big\rangle$ are summed). Using Eq. (8), one can show that for any λ, $\boldsymbol{k}$ mode the probability of finding all possible numbers of photons in a coherent state is unity (*i.e.*, $|\alpha_\lambda(\boldsymbol{k})\rangle$ is normalized):

$$\sum_{n_\lambda(\boldsymbol{k})} \left| \langle n_\lambda(\boldsymbol{k}) | \alpha_\lambda(\boldsymbol{k}) \rangle \right|^2 = 1 . \tag{29}$$

In other words, the unscattered photons have no influence on the scattering probability, provided all unscattered photons are collected without discrimination (*i.e.*, no correlations between the photons are measured.)

For the molecules, we assume that the ensemble of molecules is homogeneous in the transverse direction (with respect to the propagation direction of the x-ray pulses) and that its transverse dimension is much larger than the transverse size of x-ray pulses, so the ensemble average over $\boldsymbol{b}_\perp$ can be performed readily [63, 64]:

$$\begin{aligned} &\int d\boldsymbol{b} \, \rho(\boldsymbol{b}) \, e^{i(\boldsymbol{k}'_a - \boldsymbol{k}_a)\cdot \boldsymbol{b}} \dots \\ &= (2\pi)^2 \rho_\perp \, \delta(\boldsymbol{k}'_{a\perp} - \boldsymbol{k}_{a\perp}) \int db_\parallel \, \rho_\parallel(b_\parallel) \, e^{i(k'_{a\parallel} - k_{a\parallel}) b_\parallel} \dots , \end{aligned} \tag{30}$$

where $\boldsymbol{k}_a$ and $\boldsymbol{k}'_a$ are two momentum components of the molecular wave packet [see Eq. (11)], and the ellipsis denotes the part of the differential probability independent of $\boldsymbol{b}_\perp$. The ensemble density has also been written as a product, $\rho(\boldsymbol{b}) = \rho_\perp \times \rho_\parallel(b_\parallel)$, of a homogeneous part $\rho_\perp$ and a longitudinal part $\rho_\parallel$. The expression for $\rho_\parallel(b_\parallel)$ depends on the experimental geometry and the pump procedure. In order to carry out the $b_\parallel$ integral, we assume $\rho_\parallel$ is a Gaussian distribution of width σ_b, *i.e.*, $\rho_\parallel(b_\parallel) = e^{-b_\parallel^2/2\sigma_b^2}/\sqrt{2\pi}\sigma_b$. Recall that the pump time t_a of a target at position $\boldsymbol{b}$ depends on $b_\parallel$ for co-propagating pump and probe pulses [see Eq. (12)]. Thus, the integral on the right-hand side of Eq. (30) gives

$$\begin{aligned} &\int db_\parallel \, \rho_\parallel(b_\parallel) \, e^{i(k'_{a\parallel} - k_{a\parallel}) b_\parallel} \, e^{i(\varepsilon_{n'} - \varepsilon_n) t_a} \dots \\ &\simeq e^{i(\varepsilon_{n'} - \varepsilon_n) t_d} \, e^{-\frac{1}{2}\sigma_b^2 \left(k'_{a\parallel} - k_{a\parallel} - \frac{\varepsilon_{n'n}}{c}\right)^2} \dots , \end{aligned} \tag{31}$$

where ε_n and $\varepsilon_{n'}$ are two energy components of the target superposition state [see Eq. (11)], $\varepsilon_{n'n} \equiv \varepsilon_{n'} - \varepsilon_n$, and the ellipses denote factors in $d\mathscr{P}/d\hat{\boldsymbol{k}}_1$ that are independent of $b_\parallel$. This term takes account of the uncertainty in the collision time due to the group-velocity mismatch between the pump and probe pulses as they propagate through the ensemble. However, for a dilute, longitudinally confined gas ensemble, this effect is negligible.

The remaining integrals in the EADP can be performed using the δ functions resulting from the conservation laws [see Eq. (24)] and from the $\boldsymbol{b}_\perp$ ensemble average [see Eq. (30)] in a manner analogous to that for the case of ultrafast electron diffraction [51, 53]. Thus, we do not repeat the calculations here but simply present the final expression and discuss its physical interpretation:

$$\begin{aligned} \left\langle \frac{d\mathscr{P}}{d\hat{\boldsymbol{k}}_1} \right\rangle \simeq{}& \frac{\rho_\perp}{\langle N_\gamma \rangle} \frac{1}{m_e^2 \, c^4} \sum_{\lambda_1} \left| \epsilon^*_{\lambda_1} \cdot \epsilon_{\lambda_0} \right|^2 \sum_m \sum_{n'n} \int d\boldsymbol{k}_0 \, d\boldsymbol{k}_a \\ &\times \frac{\omega_1}{\sqrt{\omega_0 \, \omega'_0}} \, \alpha^*_{\lambda_0}(\boldsymbol{k}_{0\perp}, k_{0\parallel} - \Delta k) \, \alpha_{\lambda_0}(\boldsymbol{k}_0) \\ &\times a^*(\boldsymbol{k}_{a\perp}, k_{a\parallel} + \Delta k) \, a(\boldsymbol{k}_a) \, c^*_{n'} \, c_n \, T^*_{mn'} \, T_{mn} \\ &\times e^{i(\varepsilon_{n'} - \varepsilon_n) t_d} \, e^{-\frac{1}{2}\sigma_b^2 \, (\Delta k - \frac{\varepsilon_{n'n}}{c})^2} . \end{aligned} \tag{32}$$

The amplitudes $\alpha_{\lambda_0}(\boldsymbol{k}_0)$, $a(\boldsymbol{k}_a)$, c_n, and T_{mn} appear in pairs because of the absolute square of $\mathscr{T}_{fi}$ in Eq. (26). Since the collision couples the energy and momentum components of the x-ray pulse and the molecular wave packet, the longitudinal components of $\alpha_{\lambda_0}(\boldsymbol{k}_0)$ and $a(\boldsymbol{k}_a)$ are shifted relative to their complex-conjugated counterparts by $\mp\Delta k$. The amount of the shift Δk is determined by the energy exchange between the photon and the molecule due to inelastic transitions. In particular, under the paraxial approximation and negligible molecular kinetic energies E_a and E_b, $\Delta k \simeq \varepsilon_{n'n}/c$. The factor $m_e^{-2} \, c^{-4} \sum |\epsilon^*_{\lambda_1} \cdot \epsilon_{\lambda_0}|^2$ is the Thomson differential cross section for polarized radiation.

While the final expression (32) seems complicated, as discussed in Refs. [51, 53] a concise expression connecting the EADP and the molecular motion can be obtained

under the following conditions: (i) If the duration of the x-ray pulse is shorter than the characteristic time scale of the molecular motion, Δk is smaller than the width of the spectrum $\alpha_\lambda(\boldsymbol{k})$ and, therefore, $\alpha_\lambda(k_{0\parallel} - \Delta k) \simeq \alpha_\lambda(k_{0\parallel})$. (ii) The molecule is localized such that its momentum amplitude $a(\boldsymbol{k}_a)$ is also insensitive to the variation Δk. (iii) The central frequency of the x-ray pulse is much larger than its bandwidth (*i.e.*, it has high monochromaticity) such that T_{mn} is insensitive to the variation of $\boldsymbol{k}_0$ and $\boldsymbol{k}_a$ in the wave-packet integrals, so that it can be approximately evaluated at the central momenta of $\boldsymbol{k}_0$ and $\boldsymbol{k}_a$ and then pulled out of the wave-packet integrals. Under these conditions, the expression (32) factorizes and the resultant EADP is simply proportional to

$$\left\langle \frac{d\mathscr{P}}{d\hat{\boldsymbol{k}}_1} \right\rangle \propto \sum_m \Big| \sum_n c_n \, T_{mn} \, e^{-i\varepsilon_n t_d} \Big|^2 , \tag{33}$$

which shows that time-resolved x-ray diffraction provides a mechanism by which the scattering maps the time-dependent molecular state, $\sum_n c_n \, \phi_n \, e^{-i\varepsilon_n t}$, at the moment of collision t_d to some final state m. Then the transition probabilities to the final states m are summed incoherently.

Since the EADP (32) is presented in terms of a momentum integral over the spectrum $\alpha_{\lambda_0}(\boldsymbol{k}_0)$, in order to understand further its physical interpretation we discuss next the physical meaning of the spectrum.

F. Coherent state and momentum amplitude

A coherent state provides a momentum interpretation of the spectrum $\alpha_\lambda(\boldsymbol{k})$ for the entrance state $|\alpha_0\rangle$ of the x-ray pulses. Observe that the expectation value of the linear momentum operator of the field [see Eq. (23.29) of Ref. [62]],

$$\mathcal{P} = \frac{1}{2\pi c} \int d\boldsymbol{x} \, \boldsymbol{E}^{(-)}(\boldsymbol{x}, t) \times \boldsymbol{B}^{(+)}(\boldsymbol{x}, t) \, , \tag{34}$$

in the x-ray entrance state, $|\alpha_0\rangle$, is

$$\langle \alpha_0 | \, \mathcal{P} \, | \alpha_0 \rangle = \sum_{\lambda_0} \int d\boldsymbol{k}_0 \; \boldsymbol{k}_0 \, |\alpha_{\lambda_0}(\boldsymbol{k}_0)|^2 \, . \tag{35}$$

Therefore, $|\alpha_\lambda(\boldsymbol{k})|^2$ can be identified as the momentum density of $|\alpha_0\rangle$ for the polarization λ. The superscripts $(-)$, $(+)$ in Eq. (34) stand for the negative and positive frequency components of the field operators, respectively.

In order to associate the spectrum $\alpha_\lambda(\boldsymbol{k})$ with the electric field of the x-ray pulse (which satisfies the Maxwell equations), we make the following hypothesis. Since we have modeled the x-ray pulses as composed of coherent states, it is natural to identify the expectation value of the electric field in the state $|\alpha_0\rangle$ with the classical electromagnetic radiation $\mathscr{E}(\boldsymbol{x}, t)$:

$$\langle \alpha_0 | \boldsymbol{E}(\boldsymbol{x}, t) | \alpha_0 \rangle = \mathscr{E}(\boldsymbol{x}, t) \, . \tag{36}$$

With the above identification $|\alpha_0\rangle \leftrightarrow \mathscr{E}(\boldsymbol{x}, t)$, one can connect the amplitude $\alpha_\lambda(\boldsymbol{k})$ to the waveform of the radiation by applying Eqs. (7) and (18). Therefore, one has [see also Eq. (7.91) of Ref. [65]]

$$\alpha_\lambda(\boldsymbol{k}) = \frac{-i}{8\pi^2\sqrt{\omega}} \int d\boldsymbol{x} \, e^{-i\boldsymbol{k}\cdot\boldsymbol{x}} \times \epsilon_\lambda(\boldsymbol{k}) \cdot \left(\mathscr{E}(\boldsymbol{x}, 0) + \frac{i}{\omega} \frac{\partial \mathscr{E}}{\partial t}(\boldsymbol{x}, 0) \right) . \tag{37}$$

If $\mathscr{E}(\boldsymbol{x}, t)$ is a plane wave, *e.g.*, $\cos(\boldsymbol{k}' \cdot \boldsymbol{x} - \omega' t)$, then one can show that $\alpha_\lambda(\boldsymbol{k})$ is proportional to the distribution $\delta(\boldsymbol{k} - \boldsymbol{k}')$, which is consistent with the conventional hypothesis that the photon field corresponding to a plane wave carries momentum $\hbar\boldsymbol{k}$.

III. SIMULATION DETAILS

In this section, the above theoretical model is applied to cases in which the ro-vibrational motions of diatomic molecules are imaged by coherent x-ray pulses and details of our simulations are presented. In order to make numerical calculations manageable, approximations specific to the case considered here are assumed.

A. Diatomic molecular wave functions

The Born-Oppenheimer approximation is employed to describe the molecular eigenstates, so the molecular wave function ϕ_n is factorized into a product of electronic and nuclear parts, and the nuclear part is further separated into vibrational and rotational parts. Accordingly, the quantum number $n = \{n_e, v, J, M\}$ is the collection of electronic (n_e), vibrational (v), and rotational (J, M) quantum numbers. For a diatomic molecule, one can write

$$\phi_n = \xi_{n_e}(\{\boldsymbol{y}_i\}; \boldsymbol{R}) \, \frac{u_{vJ}(\boldsymbol{R})}{|\boldsymbol{R}|} \, Y_{JM}(\hat{\boldsymbol{R}}) \, , \tag{38}$$

where $\{\boldsymbol{y}_i\}$ denotes the collection of the electrons' coordinates in the molecular frame, $|\boldsymbol{R}|$ is the internuclear distance of the molecule, ξ_{n_e} and u_{vJ} are, respectively, the electronic and vibrational parts of the wave function, and Y_{JM} is the spherical harmonic describing the rotational part of the wave function.

The molecular potential energy curves are obtained from either the literature or quantum chemistry simulations. The vibrational wave functions are calculated using the Fourier grid Hamiltonian method [66].

B. Incident x-ray pulses

We consider the x-ray pulse has an axially symmetric Gaussian profile propagating in the x direction with

velocity c:

$$\mathscr{E}(\boldsymbol{x},t) = \boldsymbol{E}_0\, e^{-\frac{y^2+z^2}{2\sigma_{yz}^2}}\, e^{-\frac{(x-ct)^2}{2\sigma_x^2}}\, \cos\big(\kappa_0(x-ct)\big)\,, \quad (39)$$

where $\boldsymbol{E}_0$ is the peak electric field, σ_{yz} and σ_x are the respective Gaussian widths in the transverse and longitudinal directions, and κ_0 is the central wave number. Substituting Eq. (39) into Eq. (37), the corresponding spectrum of $|\alpha_0\rangle$ is

$$\alpha_\lambda(\boldsymbol{k}) \simeq -i\,\frac{\sigma_{yz}^2\sigma_x}{\sqrt{8\pi c\kappa_0}}\, e^{-\frac{1}{2}\sigma_{yz}^2(k_y^2+k_z^2)}\, e^{-\frac{1}{2}\sigma_x^2(k_x-\kappa_0)^2} \times \epsilon_\lambda\cdot\boldsymbol{E}_0\,. \quad (40)$$

Here we have assumed that the width of the momentum amplitude is much smaller than its central wave number κ_0 (*i.e.*, $\sigma_x\kappa_0 \gg 1$) and that the pulses are well collimated. From Eq. (40), one sees that the momentum amplitude $\alpha_\lambda(\boldsymbol{k})$ has a Gaussian profile centered at κ_0 with a width reciprocal to the length of the x-ray pulse; also, its magnitude is proportional to the electric field amplitude.

In our simulations the x-ray pulses are linearly polarized and have a central frequency of 59.3 keV ($\kappa_0 \simeq 15.9$ a.u.). The full-width-at-half-maximum (FWHM) duration of the intensity profile is 1.00 fs ($\sigma_x \simeq 3.40\times10^3$ a.u.).

C. Transition amplitudes

The transition amplitude T_{mn} for a diatomic molecule can be calculated by substituting the molecular wave functions (38) into Eq. (25):

$$T_{mn} \simeq \sum_{i=1}^{N_e}\int d\boldsymbol{R}\, d\{\boldsymbol{y}_i\}\, e^{i\boldsymbol{q}\cdot\boldsymbol{y}_i}\,\xi_{n_b}^*\,\xi_{n_a} \times \frac{1}{\boldsymbol{R}^2}\, u_{v_bJ_b}^*\, u_{v_aJ_a}\, Y_{J_bM_b}^*\, Y_{J_aM_a}\,, \quad (41)$$

where the subscripts a and b of the quantum numbers indicate the initial and final states, respectively. In order to show that the VOC can be caused exclusively by nuclear motion, we neglect the distortion of the density of the valence electrons of each atom due to the binding force and assume that the electronic degree of freedom is frozen during the collision (*i.e.*, $n_b = n_a$). Therefore, the electron densities are still isotropic and centered at their nuclei, and any time-dependent phenomenon in the diffraction images is associated with the nuclear motion. Accordingly, the x-ray scattering from the electronic state can be considered as a summation of elastic scatterings from the electrons in the constituent atoms in the molecule:

$$\sum_{i=1}^{N_e}\int d\{\boldsymbol{y}_i\}\, e^{i\boldsymbol{q}\cdot\boldsymbol{y}_i}\,\xi_{n_b}^*\,\xi_{n_a} \simeq \sum_{j=1}^{2} f_j(\boldsymbol{q})\, e^{i\boldsymbol{q}\cdot\boldsymbol{R}_j}\,, \quad (42)$$

where $f_j(\cdot)$ is the atomic form factor of the jth atom, and $\boldsymbol{R}_j$ is the position vector of the jth atom from the origin of the center-of-mass frame of the molecule. The atomic form factors $f_j(\cdot)$ are obtained from Ref. [55]. Whereas the scattering signals from electronically inelastic scattering (*i.e.*, $n_b \neq n_a$) may be significant for light molecules, the contribution of such inelastic scattering signals can in principle be reduced by means of energy-resolved measurements, provided there is adequate energy resolution. Owing to our focus on VOC due to the motions of the atoms in a molecule, our formulation does treat inelastic transitions between molecular states.

After applying Eq. (42), the $\boldsymbol{R}$ integral of Eq. (41) can be performed by using the plane-wave expansion of $e^{i\boldsymbol{q}\cdot\boldsymbol{R}_j}$ (as done in Ref. [51]), so that the integral is separated into radial and angular parts. The angular part yields a spherical harmonic and a product of Wigner $3j$-symbols, which are calculated using the package of Ref. [67]. The radial part involves integrations of the vibrational wave functions and spherical Bessel functions. The Bessel functions are generated using a continued fraction technique [68]. The radial integrals are then calculated numerically.

D. Molecular scattering intensities

After calculating the transition amplitudes T_{mn}, the EADP can be computed using Eq. (32). Since we have assumed the paraxial approximation for the x-ray pulses in our model (see Sec. II E), the distribution of the transverse components of $\alpha_\lambda(\boldsymbol{k})$ [see Eq. (40)] is narrow and, hence, T_{mn} is insensitive to the variation of $\boldsymbol{k}_{0\perp}$ within the width of σ_{yz}. Therefore, T_{mn} is approximated by evaluating it at $\boldsymbol{k}_{0\perp} \simeq 0$ a.u., and then the $\boldsymbol{k}_{0\perp}$ integral can be calculated analytically. The longitudinal part of the wave-packet integral for the x ray is integrated numerically using the Gauss-Hermite quadrature.

We assume that the molecule has zero initial velocity and is localized in space, so the width of its momentum amplitude $a(\boldsymbol{k}_a)$ is broad enough such that $a(\boldsymbol{k}_{a\perp}, k_{a\parallel}+\Delta k) \simeq a(\boldsymbol{k}_a)$. We further assume that T_{mn} is insensitive to the variation of $\boldsymbol{k}_a$ within the range of the wave-packet integral. Thus, the $\boldsymbol{k}_a$ integral can also be calculated analytically. In order to further simplify the numerical calculations, we use the approximation that, given the initial molecular state (v_a, J_a), final vibrational state v_b, and the angular momentum transfer ΔJ in the scattering, the radial part of T_{mn} is insensitive to the final angular momentum J_b. Therefore, the closure relation of the spherical harmonics is used in the final-state sum over (J_b, M_b) of the EADP. The validity of this approximation can be assessed by inspecting the significance of the rotational motion to the vibrational levels through the centrifugal energy $J(J+1)/(2\mu\boldsymbol{R}^2)$ of the vibrational states $u_{vJ}(\boldsymbol{R})$, where μ is the reduced mass of the diatomic molecule. Since the energy interval between adjacent rotation states of a rigid rotor is proportional to J/μ, the approximation is good for low-lying rotational states and

for heavy molecules. In addition, since the centrifugal barrier is more substantial as $\boldsymbol{R} \to 0$, the approximation is worse for highly-excited vibrational states which are more delocalized. The typical ranges of the vibrational and rotational transitions that we take into account for each component of the wave packets for the two diatomic molecules we treat are $\Delta v \leq 40$ and $\Delta J \leq 50$, respectively.

Finally, since the EADP includes transitions that are independent of the time delay [*i.e.*, terms with $n' = n$ in Eq. (32)], they can be removed in order to accentuate the delay-dependent interference terms (which are called *molecular scattering intensities* in time-independent coherent diffraction) by the following procedures. First, the two-dimensional angular distribution of the EADP at each pump-probe delay is reduced to a one-dimensional distribution in momentum transfer q by integrating over the azimuthal scattering angle φ [see Fig. 2(a) for the definition of φ.] Second, since the delay-independent baseline is approximately proportional to the sum of scattering intensities $|f_1(\boldsymbol{q})|^2 + |f_2(\boldsymbol{q})|^2$ from both atoms (*i.e.*, the atomic scattering intensities), the reduced one-dimensional distribution is fitted to $|f_1(\boldsymbol{q})|^2 + |f_2(\boldsymbol{q})|^2$ in order to obtain the proportionality factor. Then the proportionality factors of all delays are averaged, and the averaged factor is used to remove the baseline from all two-dimensional angular distributions. Finally, the baseline-subtracted angular distributions are further divided by $|f_1(\boldsymbol{q})||f_2(\boldsymbol{q})|$ in order to compensate for the decrease of scattering intensities at large momentum transfer q. Note also that the scattering from the ground molecular state is neglected, for its images are static in our model. Moreover, the polarization factors (*i.e.*, the Thomson differential cross sections) are also removed from the EADPs.

IV. TIME-RESOLVED X-RAY DIFFRACTION FROM VIBRATING MOLECULES

As noted in Sec. I, one feature of our model of time-resolved coherent x-ray scattering is that the time-resolved diffraction images from a coherent molecular motion are not necessarily centrosymmetric. We have found that the VOC is more pronounced for large-amplitude vibrations of light molecules. Hence, in this section we present numerical results for two examples of light diatomic molecules. In Sec. IV A deuterated lithium hydride, LiD, is chosen to illustrate the VOC. In Sec. IV B we show that the VOC is not limited to heteronuclear molecules, but can also be observed as an isotope effect of a homonuclear diatomic molecule. Results are thus given for the deuterated hydrogen molecule, HD.

A. Deuterated lithium hydride (LiD)

Deuterated lithium hydride, LiD, is chosen rather than lithium hydride, LiH, in order to increase the time scale of the light molecule's vibrational motion. Orientation of LiD is necessary, for the heterogeneity of the two atoms alone is insufficient to break the inversion symmetry. Figure 1 shows the potential energy curves of the $X^1\Sigma^+$ and $A^1\Sigma^+$ states of LiD. The potential curves are obtained from Ref. [69] and are cross-checked using the complete active-space self-consistent field method involving a 6-311G basis set provided by the Gaussian 16 package [70]. One sees that the $A^1\Sigma^+$ state supports an oscillation of the bond length between 3 to 8 a.u. The inset of Fig. 1 shows the Franck-Condon factors for the ro-vibrational transitions $(v'' = 0, J'' = 0) \to (v' = v, J' = 1)$. At time zero, the molecule is prepared in a coherent state [*i.e.*, defined by the c_n in Eq. (11)] such that two-thirds of the excited population is in the $J' = 0$ state and the rest is in the $J' = 1$ state with $M' = 0$ for both Js; also, the vibrational states for $J' = 0$ and 1 are given by their respective Franck-Condon factors.

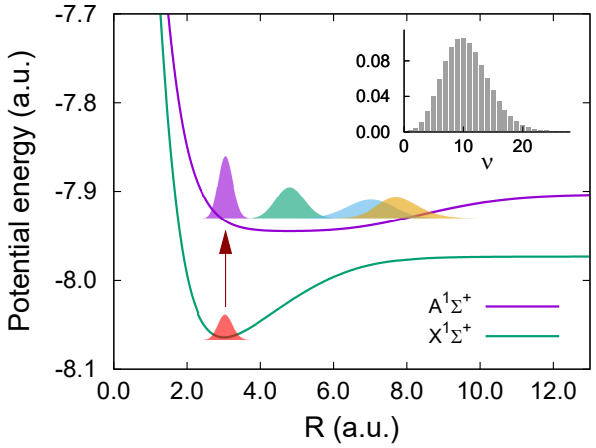

FIG. 1. Molecular potential energy curves for the $X^1\Sigma^+$ and $A^1\Sigma^+$ states of lithium hydride. The molecule undergoes a vertical transition caused by some pump procedure, and the ensuing ro-vibrational motion of the excited molecular wave packet is imaged by short x-ray pulses as a function of pump-probe delay. The inset shows the Franck-Condon factors as a function of the vibrational number v of the $A^1\Sigma^+$ state for the ro-vibrational transition $J'' = 0 \to J' = 1$.

The right column of Fig. 2 shows the weighted density distribution of the ro-vibrational wave packet in the $A^1\Sigma^+$ state in the upper half of the plane perpendicular to the propagation direction of the x-ray pulses as a function of time after the pump pulse. The probability density of the wave packet is multiplied by the square of the internuclear distance $\boldsymbol{R}^2$ to compensate for the decrease of the density as the internuclear distance increases. At time zero, the wave packet is localized about a bond length of 3 a.u. with an oriented angular distribution. The nuclear coordinate $\boldsymbol{R}$ is that of the D atom with respect to the Li atom and the LiD molecule is oriented so that the majority of the molecules have the D atom to the right of the Li atom. As time increases, the wave packet propagates outward and spreads. The wave

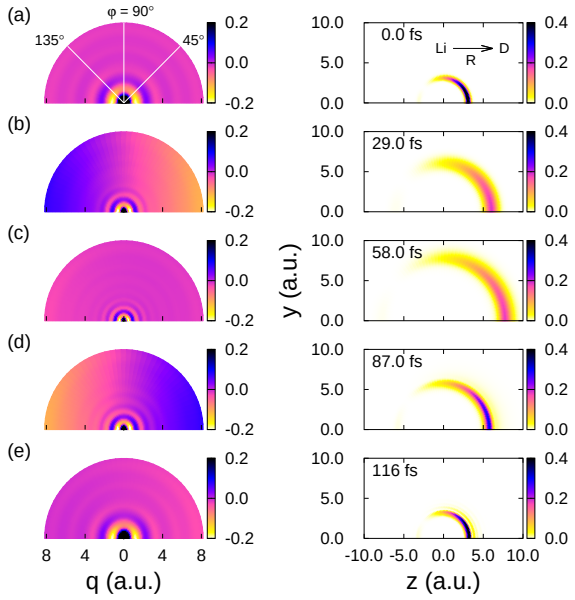

FIG. 2. *Right column*: Density distribution of the molecular wave packet of LiD in the $A^1\Sigma^+$ state in the yz plane as a function of time after the pump pulse. The molecular axis (from Li to D atoms) is oriented such that the axes of the majority of molecules point toward positive z. *Left column*: Time-resolved molecular scattering intensities for 1-fs (FWHM) x-ray pulses from the oriented ro-vibrational motion of LiD as a function of pump-probe delay t_d. The azimuthal scattering angle $\varphi = 0°$ corresponds to the positive z direction. Owing to symmetry, the diffraction images and molecular densities are only presented in the upper half of the yz plane.

packet reaches the outer turning point at about 58 fs and then reverses its direction of motion in the second half of the vibration. Owing to the much longer time scale of the rotational motion, no appreciable changes of the angular distribution are observed.

The left column of Fig. 2 presents the *molecular scattering intensities* (see Sec. III D) for 1-fs (FWHM) x-ray pulses (at pump-probe delay times, t_d, corresponding to those of the LiD molecular motion in the right column) as functions of the magnitude of the momentum transfer, q, and the azimuthal scattering angle, φ. In time-independent scattering, the molecular scattering intensities relate directly to the geometry of the molecular target (*i.e.*, to bond lengths and angles); we expect a similar relation to hold in time-dependent scattering. The magnitude, q, of the momentum transfer is calculated from the scattering angle, θ, using $q = 2\kappa_0 \sin(\theta/2)$, where κ_0 is the central momentum of the x-ray pulses.

At zero pump-probe delay [Fig.2(a)], the diffraction image shows a concentric ring pattern with the scattering intensities peaking along the orientation axis (*i.e.*, $\varphi = 0°$ and 180°). (This peaking is most easily seen for the innermost ring.) Similarly to a Young's double-slit interference pattern, the ring patterns in Fig. 2 result from the interference of the scattering amplitudes

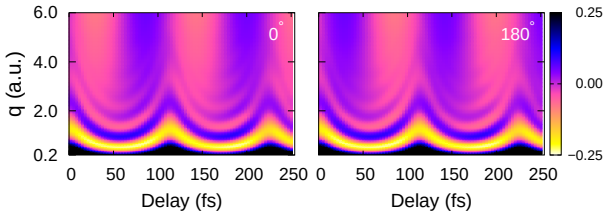

FIG. 3. Comparison of the molecular scattering intensities at azimuthal scattering angles $\varphi = 0°$ and 180° as a function of pump-probe delay. Note that the time-varying scattering intensities of the left and right panels oscillate out of phase for $q \geq 3.0$ a.u.

from the Li and D atoms, with the stronger intensities along $\varphi = 0°$ and 180° due to the molecular orientation. (See Ref. [71] for the diffraction patterns resulting from ultrafast electron diffraction from aligned–not oriented–molecules.) As the atoms move outward [see Fig. 2(b)], the rings shrink toward the center, and the contrast of the ring pattern is reduced at larger momentum transfers ($q \gtrsim 4$ a.u.). The loss of contrast is mainly due to the spread of the wave packet and the higher sensitivity of the interference fringes at large q to the variation of the internuclear distance.

In addition to the ring pattern, one clearly sees that the scattering intensities are asymmetric, with more x-ray photons scattered toward $\varphi > 90°$ at large momentum transfer. After the direction of motion reverses at $t_d = 58$ fs, the asymmetry changes sign [see Fig. 2(d)]. Figure 3 shows a detailed comparison of the scattering intensities at $\varphi = 0°$ and 180° with a finer time-delay step, and Fig. 4 presents the corresponding asymmetry of the EADP for six different time delays. The asymmetry is defined as the difference of the EADP at $\varphi = 0°$ and 180° normalized by their sum:

$$Asymmetry \equiv \frac{d\mathscr{P}(\varphi = 0°) - d\mathscr{P}(\varphi = 180°)}{d\mathscr{P}(\varphi = 0°) + d\mathscr{P}(\varphi = 180°)}, \quad (43)$$

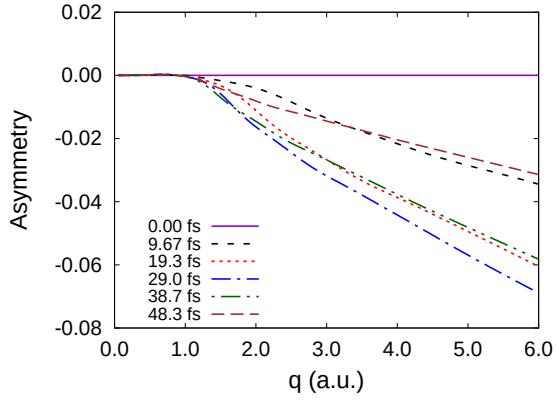

FIG. 4. Asymmetry of the EADP for the LiD molecule as a function of momentum transfer q for six different time delays. The asymmetry is defined in Eq. (43).

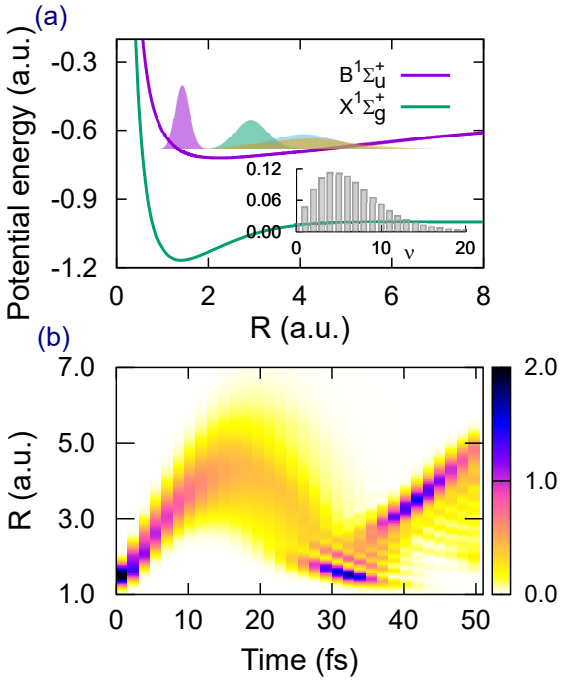

FIG. 5. (a) Molecular potential curves of the $X^1\Sigma_g^+$ and $B^1\Sigma_u^+$ states of the hydrogen molecule. The inset shows the Franck-Condon factors for the ro-vibrational transitions $(v''=0, J''=0) \rightarrow (v'=v, J'=1)$. (b) Radial density distribution of the oriented ro-vibrational motion of HD in the $B^1\Sigma_u^+$ state as a function of time.

where $d\mathscr{P}$ denotes the EADP. Note that the molecular densities are asymmetric throughout the molecular motion, and no asymmetry can be discerned when the wave packet reaches the turning points [see Figs. 2(a), (c), and (e)], indicating that the asymmetry is related to the molecular motion rather than to the relative positions of the nuclei.

B. Deuterated hydrogen molecule (HD)

The VOC demonstrated above for the LiD molecule is not limited to heteronuclear molecules. In fact, the asymmetry can also be observed as an isotope effect in the case of a homonuclear diatomic molecule. To demonstrate this, we consider here time-resolved coherent x-ray diffraction from the same type of ro-vibrational molecular motion for the case of the deuterated hydrogen molecule (HD) in its $B^1\Sigma_u^+$ state. The hydrogen molecule is chosen because of its strong isotope effect. Figure 5(a) shows the molecular potential curves of the ground $X^1\Sigma_g^+$ and excited $B^1\Sigma_u^+$ states. The inset figure shows the corresponding Franck-Condon factors for the $(v''=0, J''=0) \rightarrow (v'=v, J'=1)$ transitions. The potential curves are calculated using the same method used for the LiD case. In order to simplify the numerical calculation, the potential curve for the excited state is slightly shifted toward the origin by 0.13 a.u.

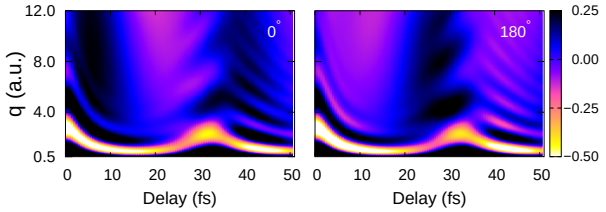

FIG. 6. Molecular scattering intensities for 1-fs (FWHM) x-ray pulses from the molecular ro-vibrational motion of HD as a function of pump-probe delay time, t_d, at azimuthal scattering angles $\varphi = 0°$ and 180°.

The radial density distribution of the molecular wave packet in the $B^1\Sigma_u^+$ state as a function of time is shown in Fig. 5(b). In this case, the nuclear coordinate $\boldsymbol{R}$ is the coordinate of the H atom with respect to the D atom. For the purpose of comparison, we assume the orientation of the HD molecules has the same angular distribution as in the case of LiD.

Figure 6 compares the molecular scattering intensities at the azimuthal scattering angles $\varphi = 0°$ and 180° as a function of pump-probe delay time, t_d. The scattering intensities clearly show an asymmetry, and the sign of the asymmetry is associated with the direction of molecular motion shown in Fig. 5(b). Specifically, the asymmetry between the diffraction images for $\varphi = 0°$ and 180° for delay times $0 \leq t_d \leq 15$ fs as well as for $30 \leq t_d \leq 45$ fs during which the molecule is expanding contrasts with the opposite asymmetry in the diffraction pattern for $15 \leq t_d \leq 30$ fs when the molecule is contracting [see Fig. 5(b)]. Note that the asymmetry is solely due to the motion of the atoms, not their heterogeneity because, in our model, the two hydrogen atoms have the same electron density (and hence the same atomic form factor), but as they vibrate the H and D atoms have different velocities owing to their mass difference.

Comparison of the scattering intensities for the LiD and HD molecules indicates some differences. First, the signs of the asymmetry are opposite. Note that in both cases the nuclear coordinates $\boldsymbol{R}$ point from the heavy atom to the light one, and both molecules are oriented with the same angular distribution. In the LiD case, more photons are scattered in the same direction of motion of the heavier atom (Li) [see Figs. 2(b) and 2(d)], but the opposite occurs for the HD case [compare the asymmetries in Figs. 3 and 6]. This is because although the D atom has a larger speed during the vibration, the stronger scattering intensity from the Li atom dominates the asymmetry. Second, the interference fringes of HD show stronger contrast at larger momentum transfer [compare Figs. 3 and 6]. This results from the equal magnitude of the scattering amplitudes from both hydrogen atoms for HD, whereas in LiD the scattering amplitude for the D atom decays faster than that for the Li atom. Third, the interference fringes of HD have a different pattern for the second cycle $(32 \leq t_d \leq 42$ fs) of the vibra-

tion compared with that of the first cycle ($0 \leq t_d \leq 10$ fs). This is due to the stronger anharmonicity of the excited HD state $B^1\Sigma_u^+$, and this effect can also be seen in the skewed HD Franck-Condon factors, *i.e.*, having a longer tail at high v [Fig. 5(a)] and in the spread of the radial density with increasing time [Fig. 5(b)].

V. SUMMARY AND DISCUSSION

In summary, we have presented a model for the description of time-resolved coherent x-ray diffraction that we have used to image the ro-vibrational motion of oriented LiD and HD molecules. The simulations show that, in addition to the usual ring patterns originating from interference between x-rays scattered from the two atoms in the diatomic molecule, the molecular scattering intensities show asymmetric distributions whenever the motion of the two atoms breaks the inversion symmetry. The time-resolved diffractive images, therefore, are not simply a collection of images of static molecules at each time delay. Also, owing to the VOC, the time-resolved diffraction images cannot be interpreted using a charge-density interpretation as in Eq. (1), which is frequently assumed in phase-retrieval algorithms employed for molecular structural determination. However, the VOC in time-resolved x-ray scattering images provides more information than is provided in time-independent x-ray diffraction. This additional information enables one to properly interpret molecular motions and thus to elucidate reaction paths.

Although our model shows that VOC is a general phenomenon in time-resolved x-ray scattering, we have found that the asymmetry is insignificant for small amplitude vibrations of heavy diatomic molecules. The degree of the asymmetry depends on such factors as: (i) The *momentum* distribution of the molecular wave packet, and in particular its width and anisotropy; and (ii) The magnitude of the momentum transfer. In the two general cases we have treated, these factors imply specifically that VOC depends on the degree of molecular orientation as well as the mass and charge ratios of the two atoms in a diatomic molecule. The mass ratio determines the disparity of the atoms' speed as the molecule vibrates, and the charge ratio determines the relative strength of the scattering amplitudes. Note however that some of these factors tend to counteract to one other. For example, although a light atom moves faster, it usually has fewer electrons and consequently a weaker x-ray scattering intensity. These two effects can contribute to the asymmetry with opposite signs (*cf.* Figs. 3 and 6). Also, as shown for LiD and HD, the asymmetry can be appreciable at larger momentum transfers. Since ultrafast electrons carry larger momenta than x-ray photons [72–76], they may be a better probe for exploiting this VOC phenomenon in diffraction images.

It is interesting to note that the x-ray diffraction images illustrate the uncertainty relation of the complementary variables of position and momentum. Specifically, one may consider the ring pattern and the VOC asymmetry as measurements of the bond length and momenta, respectively, of the nuclei in a diatomic molecule. When the contrast of the ring pattern decreases at large q as the molecular wave packet moves and spreads (providing thereby less accuracy for the determination of the bond length), the degree of the asymmetry grows in the same region of q (providing more certainty about the direction of motion of the atoms).

Finally, since asymmetric electronic motions in atoms also produce similar asymmetric diffraction patterns [47, 51, 52, 64], the asymmetry in x-ray diffraction from diatomic molecules may be altered if electronic transitions accompany the ro-vibrational nuclear motion during a molecular reaction. Hence, the VOC asymmetry may be a probe for studying the interplay between the electronic and nuclear degrees of freedom in molecular reactions.

ACKNOWLEDGMENTS

This work was supported in part by the U.S. National Science Foundation under Grant No. PHY-1505492. This work was completed utilizing the Holland Computing Center of the University of Nebraska, which receives support from the Nebraska Research Initiative.

[1] R.W. Schoenlein, S. Chattopadhyay, H.H.W. Chong, T.E. Glover, P.A. Heimann, C.V. Shank, A.A. Zholents, and M.S. Zolotorev, Generation of Femtosecond Pulses of Synchrotron Radiation, Science **287**, 2237 (2000).

[2] S. Khan, K. Holldack, T. Kachel, R. Mitzner, and T. Quast, Femtosecond Undulator Radiation from Sliced Electron Bunches, Phys. Rev. Lett. **97**, 074801 (2006).

[3] A.G. Stepanov and C.P. Hauri, Short X-ray pulses from third-generation light sources, J. Synchrotron Rad. **23**, 141 (2016).

[4] F. Zamponi, Z. Ansari, C. von Korff Schmising, P. Rothhardt, N. Zhavoronkov, M. Woerner, T. Elsaesser, M. Bargheer, T. Trobitzsch-Ryll, and M. Haschke, Femtosecond hard X-ray plasma sources with a kilohertz repetition rate, Appl. Phys. A **96**, 51 (2009).

[5] S. Corde, K. Ta Phuoc, G. Lambert, R. Fitour, V. Malka, A. Rousse, A. Beck, and E. Lefebvre, Femtosecond x rays from laser-plasma accelerators, Rev. Mod. Phys. **85**, 1 (2013).

[6] L. Miaja-Avila, G.C. O'Neil, J. Uhlig, C.L. Cromer, M.L. Dowell, R. Jimenez, A.S. Hoover, K.L. Silverman, and J.N. Ullom, Laser plasma x-ray source for ultrafast time-resolved x-ray absorption spectroscopy, Struct. Dyn. **2**, 024301 (2015).

[7] H. Tanaka *et al.*, A compact X-ray free-electron laser emitting in the sub-ångström region, Nature Photon. **6**, 540 (2012).

[8] E. Allaria *et al.*, Highly coherent and stable pulses from the FERMI seeded free-electron laser in the extreme ultraviolet, Nat. Photon. **6**, 699 (2012).

[9] C. Pellegrini, A. Marinelli, and S. Reiche, The physics of x-ray free-electron lasers, Rev. Mod. Phys. **88**, 015006 (2016).

[10] C. Bostedt, S. Boutet, D.M. Fritz, Z. Huang, H.J. Lee, H.T. Lemke, A. Robert, W.F. Schlotter, J.J. Turner, and G.J. Williams, Linac Coherent Light Source: The first five years, Rev. Mod. Phys. **88**, 015007 (2016).

[11] E.A. Seddon *et al.*, Short-wavelength free-electron laser sources and science: a review, Rep. Prog. Phys. **80**, 115901 (2017).

[12] N. Rohringer and R. Santra, X-ray nonlinear optical processes using a self-amplified spontaneous emission free-electron laser, Phys. Rev. A **76**, 033416 (2007).

[13] L. Young *et al.*, Femtosecond electronic response of atoms to ultra-intense X-rays, Nature **466**, 56 (2010).

[14] S.-K. Son, L. Young, and R. Santra, Impact of hollow-atom formation on coherent x-ray scattering at high intensity, Phys. Rev. A **83**, 033402 (2011).

[15] C.E. Liekhus-Schmaltz *et al.*, Ultrafast isomerization initiated by X-ray core ionization, Nat. Commun. **6**, 8199 (2015).

[16] N. Berrah, Molecular dynamics induced by short and intense x-rays pulses from the LCLS, Phys. Scr. **T169**, 014001 (2016).

[17] A. Rudenko *et al.*, Femtosecond response of polyatomic molecules to ultra-intense hard X-rays, Nature **546**, 129 (2017).

[18] K.R. Ferguson *et al.*, Transient lattice contraction in the solid-to-plasma transition, Sci. Adv. **2**, e1500837 (2016).

[19] P.J. Ho, C. Knight, M. Tegze, G. Faigel, C. Bostedt, and L. Young, Atomistic three-dimensional coherent x-ray imaging of nonbiological systems, Phys. Rev. A **94**, 063823 (2016).

[20] S.P. Neville, V. Averbukh, S. Patchkovskii, M. Ruberti, R. Yun, M. Chergui, A. Stolow, and M.S. Schuurman, Beyond structure: Ultrafast X-ray absorption spectroscopy as a probe of non-adiabatic wavepacket dynamics, Faraday Discuss. **194**, 117 (2016).

[21] M. Chergui and E. Collet, Photoinduced Structural Dynamics of Molecular Systems Mapped by Time-Resolved X-ray Methods, Chem. Rev. **117**, 11025 (2017).

[22] C. Weninger, M. Purvis, D. Ryan, R.A. London, J.D. Bozek, C. Bostedt, A. Graf, G. Brown, J.J. Rocca, and N. Rohringer, Stimulated Electronic X-Ray Raman Scattering, Phys. Rev. Lett. **111**, 233902 (2013).

[23] M. Kowalewski, B.P. Fingerhut, K.E. Dorfman, K. Bennett, and S. Mukamel, Simulating Coherent Multidimensional Spectroscopy of Nonadiabatic Molecular Processes: From the Infrared to the X-ray Regime, Chem. Rev. **117**, 12165 (2017).

[24] T. Kroll *et al.*, Stimulated X-Ray Emission Spectroscopy in Transition Metal Complexes, Phys. Rev. Lett. **120**, 133203 (2018).

[25] M. Kazama, T. Fujikawa, N. Kishimoto, T. Mizuno, J. Adachi, and A. Yagishita, Photoelectron diffraction from single oriented molecules: Towards ultrafast structure determination of molecules using x-ray free-electron lasers, Phys. Rev. A **87**, 063417 (2013).

[26] D. Popova-Gorelova, J. Küpper, and R. Santra, Imaging electron dynamics with time- and angle-resolved photoelectron spectroscopy, Phys. Rev. A **94**, 013412 (2016).

[27] K.-J. Yuan and A.D. Bandrauk, Exploring coherent electron excitation and migration dynamics by electron diffraction with ultrashort X-ray pulses, Phys. Chem. Chem. Phys. **19**, 25846 (2017).

[28] H.N. Chapman and K.A. Nugent, Coherent lensless X-ray imaging, Nat. Photon. **4**, 833 (2010).

[29] J. Miao, R.L. Sandberg, and C. Song, Coherent X-ray Diffraction Imaging, IEEE J. of Selected Topics in Quantum Electronics **18**, 399 (2012).

[30] A. Barty, J. Küpper, and H.N. Chapman, Molecular Imaging Using X-Ray Free-Electron Lasers, Annu. Rev. Phys. Chem. **64**, 415 (2013).

[31] J. Miao, T. Ishikawa, I.K. Robinson, and M.M. Murnane, Beyond crystallography: Diffractive imaging using coherent x-ray light sources, Science **348**, 530 (2015).

[32] N. Jones, Crystallography: Atomic secrets, Nature **505**, 602 (2014); doi:10.1038/505602a

[33] T. Elsaesser and M. Woerner, Perspective: Structural dynamics in condensed matter mapped by femtosecond x-ray diffraction, J. Chem. Phys. **140**, 020901 (2014).

[34] J.N. Clark *et al.*, Imaging transient melting of a nanocrystal using an X-ray laser, Proc. Natl. Acad. Sci. USA **112**, 7444 (2015).

[35] M.P. Minitti *et al.*, Imaging Molecular Motion: Femtosecond X-Ray Scattering of an Electrocyclic Chemical Reaction, Phys. Rev. Lett. **114**, 255501 (2015).

[36] D. Popova-Gorelova and R. Santra, Imaging instantaneous electron flow with ultrafast resonant x-ray scattering, Phys. Rev. B **91**, 184303 (2015).

[37] J.M. Glownia *et al.*, Self-Referenced Coherent Diffraction X-Ray Movie of Ångström- and Femtosecond-Scale Atomic Motion, Phys. Rev. Lett. **117**, 153003 (2016).

[38] A.M. Lindenberg, S.L. Johnson, and D.A. Reis, Visualization of Atomic-Scale Motions in Materials via Femtosecond X-Ray Scattering Techniques, Annu. Rev. Mater. Res. **47**, 425 (2017).

[39] V. Šrajer and M. Schmidt, Watching proteins function with time-resolved x-ray crystallography, J. Phys. D **50**, 373001 (2017).

[40] J.C.H. Spence, XFELs for structure and dynamics in biology, IUCrJ **4**, 322 (2017).

[41] M. Sliwa *et al.*, Femtosecond X-Ray Diffraction Studies of the Reversal of the Microstructural Effects of Plastic Deformation during Shock Release of Tantalum, Phys. Rev. Lett. **120**, 265502 (2018).

[42] S.J. Turneaure, P. Renganathan, J.M. Winey, and Y.M. Gupta, Twinning and Dislocation Evolution during Shock Compression and Release of Single Crystals: Real-Time X-Ray Diffraction, Phys. Rev. Lett. **120**, 265503 (2018).

[43] J. Cao and K.R. Wilson, Ultrafast X-ray Diffraction Theory, J. Phys. Chem. A **102**, 9523 (1998).

[44] S. Tanaka, V. Chernyak, and S. Mukamel, Time-resolved x-ray spectroscopies: Nonlinear response functions and Liouville-space pathways. Phys. Rev. A **63**, 063405 (2001).

[45] S. Bratos, F. Mirloup, R. Vuilleumier, and M. Wulff, Time-resolved x-ray diffraction: Statistical theory and its application to the photo-physics of molecular iodine, J. Chem. Phys. **116**, 10615 (2002).

[46] U. Lorenz, K.B. Møller, and N.E. Henriksen, Theory of time-resolved inelastic x-ray diffraction, Phys. Rev. A **81**, 023422 (2010).

[47] G. Dixit, O. Vendrell, and R. Santra, Imaging electronic quantum motion with light, Proc. Natl. Acad. Sci. USA **109**, 11636 (2012).

[48] A. Kirrander, K. Saita, and D.V. Shalashilin, Ultrafast X-ray Scattering from Molecules, J. Chem. Theory Comput. **12**, 957 (2016).

[49] J.R. Rouxel, M. Kowalewski, K. Bennett, and S. Mukamel, X-Ray Sum Frequency Diffraction for Direct Imaging of Ultrafast Electron Dynamics, Phys. Rev. Lett. **120**, 243902 (2018).

[50] G. Friedel, Sur les symétries cristallines que peut révéler la diffraction des rayons Röntgen, Comptes Rendus Acad. Sci. **157**, 1533 (1913).

[51] H.-C. Shao and A.F. Starace, Imaging coherent electronic motion in atoms by ultrafast electron diffraction, Phys. Rev. A **88**, 062711 (2013).

[52] M. Simmermacher, N.E. Henriksen, and K.B. Møller, Time-resolved X-ray scattering by electronic wave packets: Analytic solutions to the hydrogen atom, Phys. Chem. Chem. Phys. **19**, 19740 (2017).

[53] H.-C. Shao and A.F. Starace, Imaging electronic motions in atoms by energy-resolved ultrafast electron diffraction, Phys. Rev. A **90**, 032710 (2014).

[54] E.U. Condon, Nuclear motions associated with electron transitions in diatomic molecules, Phys. Rev. **32**, 858 (1928).

[55] J.H. Hubbell, Wm.J. Veigele, E.A. Briggs, R.T. Brown, D.T. Cromer, and R.J. Howerton, Atomic form factors, incoherent scattering functions, and photon scattering cross sections, J. Phys. Chem. Ref. Data **4**, 471 (1975).

[56] P.J. Brown, A.G. Fox, E.N. Maslen, M.A. O'Keefe, and B.T.M. Willis, Intensity of Diffracted Intensities, in *International Tables for Crystallography, Vol C, 3rd Ed.* edited by E. Prince (Kluwer Academic Publishers, Dordrecht, 2004), Chapter 6.1, pp. 554-595.

[57] M.L. Goldberger and K.M. Watson, *Collision Theory* (John Wiley & Sons, New York, 1964).

[58] W. Greiner and J. Reinhardt, *Field Quantization* (Springer-Verlag, Berlin, Heidelberg, 1996).

[59] R.J. Glauber, Coherent and Incoherent States of the Radiation Field, Phys. Rev. **131**, 2766 (1963).

[60] E.L. Saldin, E.A. Schneidmiller, and M.V. Yurkov, *The Physics of Free Electron Lasers* (Springer-Verlag, Berlin, Heidelberg, 2000).

[61] L. Mandel and E. Wolf, *Optical Coherence and Quantum Optics* (Cambridge University Press, New York, 1995).

[62] E. Merzbacher, *Quantum Mechanics, 3rd Ed.* (John Wiley & Sons, Inc., New York, 1998).

[63] M.E. Peskin and D.V. Schroeder, *An Introduction to Quantum Field Theory* (Addision-Wesley, Reading, MA, 1995).

[64] H.-C. Shao and A.F. Starace, Energy-resolved coherent diffraction from laser-driven electronic motion in atoms, Phys. Rev. A **96**, 042706 (2017).

[65] J.D. Jackson, *Classical Electrodynamics, 3rd Ed.* (John Wiley & Sons, Inc., New York, 1998).

[66] C.C. Marston and G.G. Balint-Kurti, The Fourier grid Hamiltonian method for bound state eigenvalues and eigenfunctions, J. Chem. Phys. **91**, 3571 (1989).

[67] A.J. Stone and C.P. Wood, Root-rational-fraction package for exact calculation of vector-coupling coefficients, Comp. Phys. Comm. **21**, 195 (1980).

[68] W.J. Lentz, Generating Bessel functions in Mie scattering calculations using continued fractions, Appl. Opt. **15**, 668 (1976).

[69] H. Partridge and S.R. Langhoff, Theoretical treatment of the $X^1\Sigma^+$, $A^1\Sigma^+$, and $B^1\Pi$ states of LiH, J. Chem, Phys. **74**, 2361 (1981).

[70] M.J. Frisch *et al.*, Gaussian 16, Revision A.03, Gaussian, Inc., Wallingford CT (2016).

[71] P. Reckenthaeler, M. Centurion, W. Fuß, S.A. Trushin, F. Krausz, and E.E. Fill, Time-Resolved Electron Diffraction from Selectively Aligned Molecules, Phys. Rev. Lett. **102**, 213001 (2009).

[72] G. Sciaini and R.J.D. Miller, Femtosecond electron diffraction: heralding the era of atomically resolved dynamics, Rep. Prog. Phys. **74**, 096101 (2011).

[73] C. Kealhofer, W. Schneider, D. Ehberger, A. Ryabov, F. Krausz, and P. Baum, All-optical control and metrology of electron pulses, Science **352**, 429 (2016).

[74] J. Yang *et al.*, Diffractive Imaging of Coherent Nuclear Motion in Isolated Molecules, Phys. Rev. Lett. **117**, 153002 (2016).

[75] M. Th. Hassan, Attomicroscopy: from femtosecond to attosecond electron microscopy, J. Phys. B **51**, 032005 (2018).

[76] Y. Morimoto and P. Baum, Diffraction and microscopy with attosecond electron pulse trains, Nat. Phys. **14**, 252 (2018).